applied sciences

MDPI

Article

Prediction of Vertical Vibrations of a CNC *Router* Type Geometry

Carlos Renato Vázquez and Alejandro Guajardo-Cuéllar *

Escuela de Ingenieria y Ciencias, Tecnologico de Monterrey, Zapopan 45138, Mexico; cr.vazquez@tec.mx
* Correspondence: alejandro.guajardo@tec.mx

Featured Application: A methodology is introduced for the analytical formulation of vertical vibrations of assemblies of thin coupled beams on a plane. The method allows the fast and efficient estimation of vibration modes. It is validated and compared against the Finite Element Method and an experimental setting, and is applied for the prediction of displacement and frequencies of vertical vibrations in a CNC *router* type geometry. The method can be used to predict machine and tool proper functioning for CNC *router* machines and similar equipment.

Abstract: Mechanical vibrations represent an important problem in machining processes performed by machine tools. They affect surface quality, tool life, and productivity. In extreme situations, chattering may appear, which can dramatically reduce the tool life. CNC *router* machines are particularly sensitive to vibrations, with their structure bearing resemblance to a composition of beams that are uniform in cross-section. These CNC machines are commonly used for different tasks, like engraving, cutting, and 3D printing. This work proposes a modeling methodology for vibration systems that consist of coupled thin beams subjected to vertical vibration. This methodology is used to model vertical vibrations in a CNC *router* machine. For this, the geometry is decomposed into beams of uniform cross-sections that are coupled at their ends. Each beam is modeled by means of the classical theory of Bernoulli–Euler for thin beams. The boundary conditions are determined by the beam couplings. In the system thus defined, fundamental frequencies are calculated using the bisection method, and then the modes are computed for the corresponding frequencies. The modal amplitudes, being time-dependent, are modeled as a state space system, considering the first m frequencies. In order to provide support to the modeling methodology, simulation experiments are performed for validation, comparing the results provided by models built with the proposed methodology against finite element models and an experimental setting with a real structure. Moreover, an analysis of the vibration model focusing on a specific component of the equipment is presented to illustrate the usefulness and flexibility of the models obtained with the proposed methodology.

Keywords: vertical vibrations; modal analysis; CNC *router*

Citation: Vázquez, C.R.; Guajardo-Cuéllar, A. Prediction of Vertical Vibrations of a CNC *Router* Type Geometry. *Appl. Sci.* **2024**, *14*, 621. https://doi.org/10.3390/app14020621

Academic Editor: Rosario Pecora

Received: 30 August 2023
Revised: 16 November 2023
Accepted: 12 December 2023
Published: 11 January 2024

1. Introduction

Mechanical vibrations are present in many machine tools, affecting the cutting tool and the surface finish of the machined part. For this reason, the study of vibration behavior in machine tools has been a topic of interest. Pioneers in this topic, Minis and Yanushevsky, Altintaş and Budak [1,2], analyzed the vibrations in a machining process in the frequency domain. Minis and Yanushevsky [1] proposed a method to predict chattering in a machining process by modeling the system as a system of finite differences equations and analyzing stability via Fourier analysis. Altintas and Budak [2] presented a method to predict stability by modeling the system as a transfer function. Subsequently, many authors proposed different perspectives to analyze machining processes. More recently, Ghoshal and Bhattacharyya [3] studied the influence of vibrations in micromachining using microchemical processes. Quintana and Ciurana [4] presented a review of the state of the art about chattering. The dynamics of the cutting process and the effect in vibrations have also been investigated [5–7].

The reduction of vibrations has also received attention. Different methods have been used for this purpose. The classic passive method adds masses and damping. The semi-actives used dynamic adapting dampers and the ones used active control through the use of fast actuators to compensate for vibrations. Long et al. [8] proposed a control system for peripheral machining operations. The relative vibration between the tool and the machined part is controlled with piezoelectric actuators that adjust the part with two degrees of freedom. Similarly, Aggogeri et al. [9] proposed a mechatronic platform to actively control the vibrations of a micromachined tool of high precision using piezoelectric actuators. The frequency of the vibrations is a relevant parameter to understand the behavior of the tool. Ostasevicius et al. [10] analyzed the frequency of the vibrations during a cutting process modeling the tool as an elastic component. The vibrations at the tip of the cutting tool had an influence on the surface finish of the part; therefore, they reported that the excitation of the second vibrational flexional mode dissipated energy reducing vibrations in the system. A piezoelectric was used to excite the mode. Altintas and Khoshdarregi [11] used filters to compensate for the commands of the axes to avoid vibrations. They tested experimentally their algorithm in a table of two axes. Finally, in this effort to control the vibrations of the tool, Ford et al. [12], proposed a method to improve the performance of a machine tool controlling adaptive structural vibrations of the machine. The control system was implemented in a vertical milling machine. Deep learning techniques have also been investigated for application in monitoring and maintaining machinery that produces vibrations [13,14]. It has been of interest in the community to develop techniques that are computationally inexpensive to be implemented in equipment health monitoring by collecting data and applying algorithms in real-time [15]. The use of deep learning has great potential due to the access to data handling and acquisition, as well as the ability to process complex algorithms with reasonable computational cost in equipment maintenance. However, these methods require training and data input, limiting their use and application to situations where large data are available. In design and concept testing validation stages, methods that do not require training may be more suitable.

A particular machine sensible to mechanical vibrations is the so-called CNC *router*. The equipment RoutakitHD [16], Pro60120CNC [17], X-Carve [18], Zenbot CNC [19] are commercially available and present similar geometries. These equipment are widely used for different tasks such as cutting and engraving. Understanding the mechanical vibrations in this equipment may result in enhancing the quality of the operation and increasing the lifetime of the machine. Lou et al. [20] presented a method to evaluate the superficial quality in the machining process in a CNC *router*. Liu et al. [21] proposed a complex vibration model for the linear displacement mechanism of the power screw, a mechanism widely used in CNC machines. Experimental measurements of the vibrations in similar configurations as a CNC *router* are reported by different authors [22–25]. These investigations deal with the tool usage at different conditions including adding damping to the machine.

This work proposes a new methodology for modeling vibration systems of coupled thin beams under vertical vibration, which is later applied to a CNC *router* type geometry. The main contribution of this research is to propose and validate a method that models the vertical vibrations of a system of collinear and perpendicular beams, which are located in a plane, and the applied load is perpendicular to this plane. This arrangement is equivalent to the structure of a CNC *router*. Furthermore, since this method is an analytical solution to the model, it does not require computational effort and can be used in design stages to identify critical operating conditions of equipment subjected to vertical loads that produce vibration. Additionally, it can be used to monitor and control the mechanical vibrations of operating equipment, taking advantage of its low computational cost. The first step consists of decomposing the structure geometry into a set of coupled beams with attached masses. Next, boundary conditions are defined for the beams, considering the couplings. These conditions lead to the computation of modes for the complete structure and natural frequencies. The modal amplitudes are represented as a state-space control system. Different scenarios with different loads (e.g., constant, harmonic, time-dependent)

can be efficiently simulated with the resulting model. It is shown through numerical experiments that the obtained models are accurate when compared with a Finite Element Method (FEM) simulation, whenever the cross-section of the beams is small. Moreover, a validation based on an experimental setting with a real structure is also performed. The obtained state-space model is more suitable for control purposes in comparison to computationally expensive FEM models, particularly for CNC structures in which the model has to be updated when the tool moves. The methodology introduced here is related to other works that proposed analytical models for beams with attached masses. For instance, collinear beams with concentrated masses and coupled boundary conditions were investigated in [26,27]. Ghayesh et al. [28] studied a general solution procedure for time-dependent and nonlinear boundary conditions. They consider the concentrated masses as internal boundary conditions, and their developed method focuses on non-linear subsystems in 1-d resulting from the non-linear time-dependent boundary conditions. Rezaiee-Pajand and Hozhabrossadati [29] studied a system of two beams with elastic constraints at one end and free at the other end. The beams are coupled through a mass-spring device. The modes are analyzed for different parameters such as the spring constant of the coupling. Wu [30] presented an analysis of a Timoshenko beam with several endorsed masses for a collinear structure. An interesting analytical method for a collinear array of beams with coupled masses was developed by Liu et al. [31], the novelty of their method is that many rigid bodies can be connected to many beams in any position and orientation. Maiz et al. [32] presented an analysis of transverse vibrations of one beam with several masses added. They used the classical Bernoulli–Euler theory and calculated the fundamental frequencies and vibration modes of the assembly. An extension of this work adding the considerations of the beams theory of Rayleigh and Timoshenko, is discussed by the same group in [33]. Notice that all these works analyzed arrays of collinear beams, while in our approach we consider 2-d arrays.

The article is organized as follows. Section 2 recalls basic concepts. Section 3 presents the proposed methodology and the application to a CNC *router* structure. Section 4 shows the results of simulations and it compares the results with FEM calculations and an experimental setting. In the discussion, simulations of a particular CNC model are presented and discussed. Finally, some conclusions are provided.

2. Basic Concepts

The proposed modeling methodology is based on the classical Bernoulli–Euler theory. A CNC *router* operating properly functions within the elastic range. Any operation in the plastic range might lead to catastrophic failure. The proposed model forecasts the behavior of a CNC *router* geometry under normal operating conditions. Basic concepts and notation are presented in this section.

According to the Bernoulli–Euler theory, the behavior of vertical displacements $w(x,t)$ along a thin beam of uniform cross-section without damping, subjected to a load distribution $f(x,t)$, is described by

$$EI\frac{\partial^4 w(x,t)}{\partial x^4} + \rho A\frac{\partial^2 w(x,t)}{\partial t^2} = f(x,t) \tag{1}$$

where E is the Young modulus, I is the second moment of area, ρ is the density and A is the beam cross section area. We consider the classical solution of split variables, in which the vertical displacement is expressed as

$$w(x,t) = W(x)T(t), \tag{2}$$

Considering the unloaded case (i.e., $f(x,t) = 0$), previous expressions lead to

$$\frac{EI}{\rho A}\frac{1}{W(x)}\frac{\partial^4 W(x)}{\partial x^4} = -\frac{1}{T(t)}\frac{\partial^2 T(t)}{\partial t^2} \tag{3}$$

Since the left term is a function of x and the right term is a function of t, the only solution is that both terms are equal to a constant value, usually denoted as ω^2. The expression (3) is then split in two equations:

$$\frac{\partial^4 W(x)}{\partial x^4} = \beta^4 W(x) \tag{4}$$

$$\frac{\partial^2 T(t)}{\partial t^2} = -\omega^2 T(t) \tag{5}$$

where

$$\beta^4 = \frac{\rho A}{EI}\omega^2 \tag{6}$$

The general solution of (4) is given by

$$\begin{aligned} W(x) &= c_1 cosh(\beta x) + c_2 sinh(\beta x) + c_3 cos(\beta x) + c_4 sin(\beta x) \\ &= g(\beta, x)\mathbf{c} \end{aligned} \tag{7}$$

where

$$\begin{aligned} g(\beta, x) &= \begin{bmatrix} cosh(\beta x) & sinh(\beta x) & cos(\beta x) & sin(\beta x) \end{bmatrix} \\ \mathbf{c} &= \begin{bmatrix} c_1 & c_2 & c_3 & c_4 \end{bmatrix}^T \end{aligned} \tag{8}$$

The coefficients c_1, c_2, c_3 and c_4 depend on the boundary conditions. In fact, given a set of boundary conditions, there exist an infinite number of solutions $\mathbf{c}$ and β for (4). In particular, the solutions for β is a countable set. If the positive solutions for β are ordered as $\beta^1 < \beta^2 < \beta^3$..., for each β^k the corresponding value ω^k can be computed by (6). Such values $\omega^1 < \omega^2 < \omega^3$... are named *natural frequencies*. In this way, for each k-th natural frequency ω^k, we have a parameter β^k, and a particular vector of coefficients $\mathbf{c}^k$ can be computed such that the resulting function $W^k(x) = g(\beta^k, x)\mathbf{c}^k$ is as a solution of (4). This solution $W^k(x)$ is called the k-th *mode*.

On the other hand, given a natural frequency ω^k and particular initial conditions, the solution of (5) is denoted as $T^k(t)$, called the k-th *modal amplitude*, which can be generally described as

$$T^k(t) = a^k sin(\omega^k t) + b^k cos(\omega^k t) \tag{9}$$

where the coefficients a^k and b^k depend on the initial conditions.

In this way, the general solution for the displacement $w(x, t)$ can be expressed as

$$w(x, t) = \sum_{k=1}^{\infty} W^k(x) T^k(t) \tag{10}$$

3. Method Development

The goal of this work is to develop vibration models for structures consisting of coupled thin beams within a plane, having attached masses, and describing either orthogonal or straight angles. The model will be developed based on the Bernoulli–Euler theory for thin beams with a regular cross-section, thus it should be applied only to lean beams. It will be assumed that deformations will be maintained inside the elastic range, being coherent with practical applications, in which machines are designed for operating in this range. Elasticity in coupling components, such as bearings and ballscrews, will be neglected, since these elements are built with rigid materials and geometries. The model will only describe vertical vibrations, avoiding to consider both lateral and torsional vibrations. For this, the following modeling methodology is proposed:

1. The geometry is decomposed as a collection of thin beams coupled at the endpoints with masses attached to them.
2. Boundary conditions are established for each beam, considering couplings between sections.
3. Fundamental frequencies and modes are computed for the complete structure.
4. Load distributions are established.

5. A state space model for the modal amplitudes is obtained.

The information on the modal amplitudes and modes allows obtaining the vertical displacement at any point of the structure, by using (10).

3.1. Geometry Decomposition

In order to extend the single-beam Bernoulli–Euler solution to structures composed of several sections with attached masses, the structure is decomposed in simple regular beams. This decomposition must be defined in such a way that couplings only occur at the beam endpoints. Moreover, every pair of coupled beams must describe an angle in the set 0°, 90°, 180°, 270°. The principal axis of each beam must belong to a horizontal plane. Masses should only be attached at the beam endpoints.

The following notation will be used: e_i denotes the i-th beam, l_i denotes the length of e_i, each beam has two endpoints, the coordinate x_i will refer to the beam (local coordinate system), thus one endpoint of e_i is located at $x_i = 0$ and the other endpoint is located at $x_i = l_i$. $w_i(x_i, t)$ represents the vertical displacement of the beam e_i at local coordinate $x_i \in [0, l_i]$. E_i, G_i, I_i and J_i denote Young's modulus, the shear modulus, the cross-sectional moment of inertia, and the polar moment of inertia of e_i, respectively. Given a function $f(x)$, it will be used $f(x)|_{x'}$ to denote the evaluation of $f(x)$ at $x = x'$.

Figure 1 shows a correct decomposition in 6 simple beams for the structure of a CNC *router* type structure similar as RoutakitHD equipment [16]. Arrows on the beams indicate the local coordinate systems, i.e., the endpoint where $x_i = 0$ and the positive axis direction.

This decomposition will allow computing the modes by sections, i.e., the mode for e_i associated with the k-th fundamental frequency will be given by $W_i^k(x_i) = g(\beta_i^k, x_i)\mathbf{c}_i$, where β_i^k is related to the fundamental frequency ω^k by (6) (Notice that if some beam sections have different cross-section and/or different material, a single fundamental frequency ω^k will lead to a set of parameters $\beta_1^k, \beta_2^k, ..., \beta_m^k$, since the parameters E_i, I_i, ρ_i, A_i in (6) could be different for each beam section. In the particular case that all the beam sections have the same material and cross-section, a single parameter will be obtained for each fundamental frequency ω^k, i.e., $\beta_1^k = \beta_2^k = ... = \beta_m^k$). In this way, the set of functions

$$\{W_1^k(x_1),\ W_2^k(x_2),\ ...,\ W_n^k(x_n)\}$$

describe the k-th mode of the complete structure, associated with the frequency ω^k.

The following subsections will explain how to compute the fundamental frequencies ω^k, the corresponding parameters β_i^k and the coefficient vectors $\mathbf{c}_i^k$ for each beam element e_i, by following the aforementioned methodology.

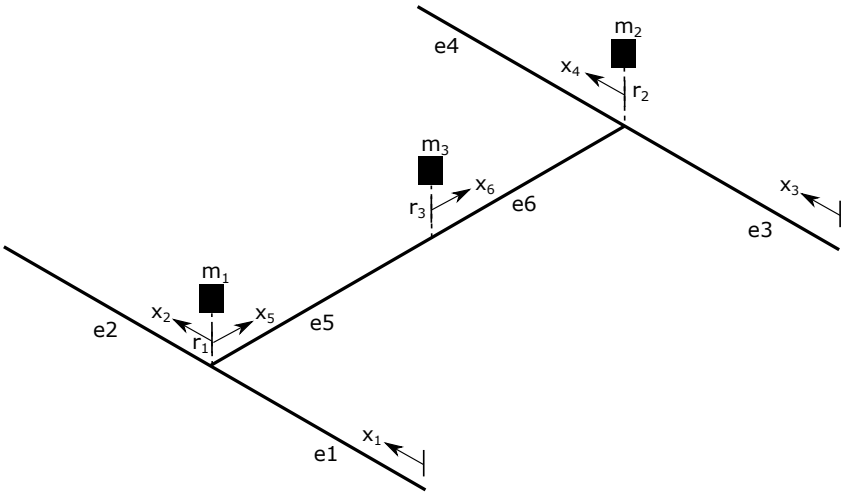

Figure 1. Decomposition of a CNC router structure similar as RoutakitHD equipment [16].

3.2. Boundary Conditions

Computing the modes for the beam sections is a coupled problem, i.e., the modes shapes of a beam depend on the modes of the other beams in the structure. This behavior results from the beam coupling, which can be described by boundary conditions. Thus, the first step in the modes computation is to establish boundary conditions for all the beams in the structure that consider the beams coupling. The beam couplings in the CNC *router* are mechanical elements, such as bearings, ballscrews and masses, which may have their own elastic properties and behavior. For this reason, masses can be attached at the coupling points in the model. However, elasticity at couplings is not considered in the model, since the elastic contribution of these components will be small because these are built with rigid geometries and materials. The relative positions of the beams studied in this work are those that a CNC *router* observes during operation, i.e., beam elements being either collinear or perpendicular.

In detail, two boundary conditions must be established for each endpoint of each beam, otherwise stated, each function $w_i(x_i, t)$ requires a total of four boundary conditions (two for each endpoint). These conditions depend on whether the beam is coupled to another beam at the endpoint or not. Figure 2 shows four possibilities of beams coupling.

An interesting feature will appear when two or more beams are perpendicularly coupled, as shown in Figure 2d). In this figure, beams e_h and e_i act as torsional springs for beams e_j and e_l, and vice versa. To compute the torsion of such springs, variables ϕ_h^e, ϕ_i^e, ϕ_j^e and ϕ_l^e (resp. ϕ_h^f, ϕ_i^f, ϕ_j^f, and ϕ_l^f) are defined to express the torsional deformation of beam e_h, e_i, e_j and e_l, respectively, at the coupling end-point (resp. at the other end-point). The sign of these angles is defined according to the right-hand rule. These torsional deformations are null at fixed and simple supported endpoints. On the other hand, they can be expressed as slopes of perpendicular beams at coupling endpoints, e.g.,

$$\phi_j^e \simeq tan(\phi_j^e) = \left.\frac{\partial w_h(x_h, t)}{\partial x_h}\right|_{x_h^e} \tag{11}$$

In the following, boundary conditions for different cases are described as both, its general formulation in terms of $w_i(x_i, t)$ and its modal formulation in terms of $W_i(x_i) = g_x(\beta_i, x_i)\mathbf{c}_i$. For this, let us denote the first, second, and third derivatives of $g(\beta_i, x_i)$ with respect to x_i as $g_x(\beta_i, x_i)$, $g_{xx}(\beta_i, x_i)$ and $g_{xxx}(\beta_i, x_i)$, respectively.

- In the case of uncoupled endpoints (e.g., $x_1 = 0$ at e_1 of Figure 1), the boundary conditions can be defined as one of the following cases:
  - Free endpoint (cantilever): there are neither bending moments nor shear forces:

$$\begin{aligned} &\text{General:} && \left.\frac{\partial^2 w_i(x_i, t)}{\partial x_i^2}\right|_{x_i^e} = 0, && \left.\frac{\partial^3 w_i(x_i, t)}{\partial x_i^3}\right|_{x_i^e} = 0, \\ &\text{Modal:} && g_{xx}(\beta_i, x_i^e)\mathbf{c}_i = 0, && g_{xxx}(\beta_i, x_i^e)\mathbf{c}_i = 0, \end{aligned} \tag{12}$$

    where x_i^e denotes the coordinate of the endpoint (thus $x_i^e = 0$ for one endpoint or $x_i^e = l_i$ for the other endpoint).
  - Fixed endpoint: there is no vertical displacement, there is no slope:

$$\begin{aligned} &\text{General:} && w_i(x_i^e, t) = 0, && \left.\frac{\partial w_i(x_i, t)}{\partial x_i}\right|_{x_i^e} = 0, \\ &\text{Modal:} && g(\beta_i, x_i^e)\mathbf{c}_i = 0, && g_x(\beta_i, x_i^e)\mathbf{c}_i = 0. \end{aligned} \tag{13}$$

– Simple supported endpoint: there is no vertical displacement, there is no bending moment:

$$\begin{aligned} &\text{General:} \quad w_i(x_i^e,t)=0, \qquad \left.\frac{\partial^2 w_i(x_i,t)}{\partial x_i^2}\right|_{x_i^e}=0, \\ &\text{Modal:} \quad g(\beta_i,x_i^e)\mathbf{c}_i=0, \qquad g_{xx}(\beta_i,x_i^e)\mathbf{c}_i=0. \end{aligned} \tag{14}$$

- Additional boundary conditions are required for endpoints at which two or more beams are coupled. These conditions depend on how many beams are coupled at the same point, if these are aligned or not, and if torsion is allowed or not. Four configurations can occur, as shown in Figure 2. The most general case involves four beams e_h, e_i, e_j and e_l, coupled at the same point, where e_h and e_i are aligned between them, e_j and e_l are perpendicular to them, and torsion is allowed. In the following, take Figure 2d) as reference. For this, the following conditions must be defined:
  – The following conditions are required to guarantee displacements continuity

$$\begin{aligned} &\text{General:} \quad w_h(x_h^e,t)=w_i(x_i^e,t)=w_j(x_j^e,t)=w_l(x_l^e,t) \\ &\text{Modal:} \quad g(\beta_h,x_h^e)\mathbf{c}_h=g(\beta_i,x_i^e)\mathbf{c}_i=g(\beta_j,x_j^e)\mathbf{c}_j=g(\beta_l,x_l^e)\mathbf{c}_l \end{aligned} \tag{15}$$

  where x_h^e, x_i^e, x_j^e, x_j^e denote the endpoints coordinates where the beams e_h, e_i, e_j, e_l are coupled.
  – The aligned beams require slope continuity, i.e.,

$$\begin{aligned} \text{General:} \quad & \left.\frac{\partial w_h(x_h,t)}{\partial x_h}\right|_{x_h^e}=\left.\frac{\partial w_i(x_i,t)}{\partial x_i}\right|_{x_i^e}, \\ & \left.\frac{\partial w_j(x_j,t)}{\partial x_j}\right|_{x_j^e}=\left.\frac{\partial w_l(x_l,t)}{\partial x_l}\right|_{x_l^e} \\ \text{Modal:} \quad & g_x(\beta_h,x_h^e)\mathbf{c}_h=g_x(\beta_i,x_i^e)\mathbf{c}_i, \\ & g_j(\beta_j,x_j^e)\mathbf{c}_j=g_x(\beta_l,x_l^e)\mathbf{c}_l \end{aligned} \tag{16}$$

  – Another condition is due to a balance of vertical forces, in detail, shear forces must be coherent with the acceleration of the mass attached at the coupling point, which is generally formulated as

$$E_hI_h\left.\frac{\partial^3 w_h(x_h,t)}{\partial x_h^3}\right|_{x_h^e}-E_iI_i\left.\frac{\partial^3 w_i(x_i,t)}{\partial x_i^3}\right|_{x_i^e}+E_jI_j\left.\frac{\partial^3 w_j(x_j,t)}{\partial x_j^3}\right|_{x_j^e} -E_lI_l\left.\frac{\partial^3 w_l(x_l,t)}{\partial x_l^3}\right|_{x_l^e}=m\frac{d^2v}{dt^2}$$

  where v is the vertical displacement of the attached mass m; if there is no mass attached at this point then the right term is substituted by 0. By using (1) and (4), the mass acceleration can be expressed in terms of the displacement at the endpoint of any of the coupled beams, e.g.,

$$\begin{aligned} \frac{d^2v}{dt^2}&=\left.\frac{\partial^2 w_h(x_h,t)}{\partial t^2}\right|_{x_h^e}=-\frac{E_hI_h}{\rho_hA_h}\left.\frac{\partial^4 w_h(x_h,t)}{\partial x_h}\right|_{x_h^e} \\ &=-\frac{E_lI_l}{\rho_lA_l}\beta_i^4 w_l(x_l^e,t) \end{aligned}$$

  The corresponding modal formulation becomes

$$E_hI_hg_{xxx}(\beta_h,x_h^e)\mathbf{c}_h-E_iI_ig_{xxx}(\beta_i,x_i^e)\mathbf{c}_i+E_jI_jg_{xxx}(\beta_j,x_j^e)\mathbf{c}_j -E_lI_lg_{xxx}(\beta_l,x_l^e)\mathbf{c}_l=-\frac{mE_hI_h}{\rho_hA_h}\beta_h^4 g(\beta_h,x_h^e)\mathbf{c}_h \tag{17}$$

– By considering the balance of moments along the longitudinal axis of beams $e_h - e_i$ and $e_j - e_l$, and the aforementioned torsional spring effects, two boundary conditions are imposed as follows

$$E_h I_h \frac{\partial^2 w_h(x_h,t)}{\partial x_h^2}\bigg|_{x_h^e} - E_i I_i \frac{\partial^2 w_i(x_i,t)}{\partial x_i^2}\bigg|_{x_i^e} - k^j\left(\phi_j^e - \phi_j^f\right) - k^l\left(\phi_l^e - \phi_l^f\right) = mr^2\frac{d^2\phi_j^e}{dt^2}$$

$$E_j I_j \frac{\partial^2 w_j(x_j,t)}{\partial x_j^2}\bigg|_{x_j^e} - E_l I_l \frac{\partial^2 w_l(x_l,t)}{\partial x_l^2}\bigg|_{x_l^e} - k^h\left(\phi_h^e - \phi_h^f\right) - k^i\left(\phi_i^e - \phi_i^f\right) = mr^2\frac{d^2\phi_h^e}{dt^2}$$

where r is the vertical distance from the neutral beam axis to the mass center of m, and $k^i = G_i J_i / l_i$ denotes the equivalent torsional elastic coefficient of e_i. The angular mass accelerations can be expressed in terms of slopes by using (1) and (4) and assuming that torsional angles are small, i.e.,

$$\frac{d^2\phi_j^e}{dt^2} \simeq \frac{\partial^2}{\partial t^2}\frac{\partial w_h(x_h,t)}{\partial x_h}\bigg|_{x_h^e} = -\frac{E_h I_h}{\rho_h A_h}\beta_i^4 \frac{\partial w_h(x_h,t)}{\partial x_h}_{h}\bigg|_{x_h^e}$$

$$\frac{d^2\phi_h^e}{dt^2} \simeq -\frac{E_j I_j}{\rho_j A_j}\beta_i^4 \frac{\partial w_j(x_j,t)}{\partial x_j}_{j}\bigg|_{x_j^e}$$

The corresponding modal formulation is

$$\begin{aligned} E_h I_h g_{xx}(\beta_h, x_h^e)\mathbf{c}_h - E_i I_i g_{xx}(\beta_i, x_i^e)\mathbf{c}_i - k^j\left(\hat{\phi}_j^e - \hat{\phi}_j^f\right) - k^l\left(\hat{\phi}_l^e - \hat{\phi}_l^f\right) &= -mr^2\frac{E_h I_h}{\rho_h A_h}\beta_h^4 g_x(\beta_h, x_h^e)\mathbf{c}_h \\ E_j I_j g_{xx}(\beta_j, x_j^e)\mathbf{c}_j - E_l I_l g_{xx}(\beta_l, x_l^e)\mathbf{c}_l - k^h\left(\hat{\phi}_h^e - \hat{\phi}_h^f\right) - k^i\left(\hat{\phi}_i^e - \hat{\phi}_i^f\right) &= -mr^2\frac{E_j I_j}{\rho_j A_j}\beta_j^4 g_x(\beta_j, x_j^e)\mathbf{c}_j \end{aligned} \tag{18}$$

where the variables $\hat{\phi}$ are the modal components of the corresponding angles ϕ, e.g., considering ϕ_j^e given by (11), we have

$$\hat{\phi}_j^e \simeq -\frac{\partial W_h(x_h)}{\partial x_h}\bigg|_{x_h^e} = g_x(\beta_h, x_h^e)\mathbf{c}_h$$

In case that torsion is not allowed, the difference between torsional angles at the end-points of any beam must null, e.g., $(\phi_j^e - \phi_j^f) = 0$, thus $(\hat{\phi}_j^e - \hat{\phi}_j^f) = 0$, which would imply that slopes at the coupling endpoints were null. Conditions (15)–(18) can be straightforwardly applied to the other configurations of Figure 2, just by removing the terms of the missing beams. Be aware that if the sense of the local coordinate system of a beam is changed, the signs of the corresponding terms in the boundary conditions must also be changed.

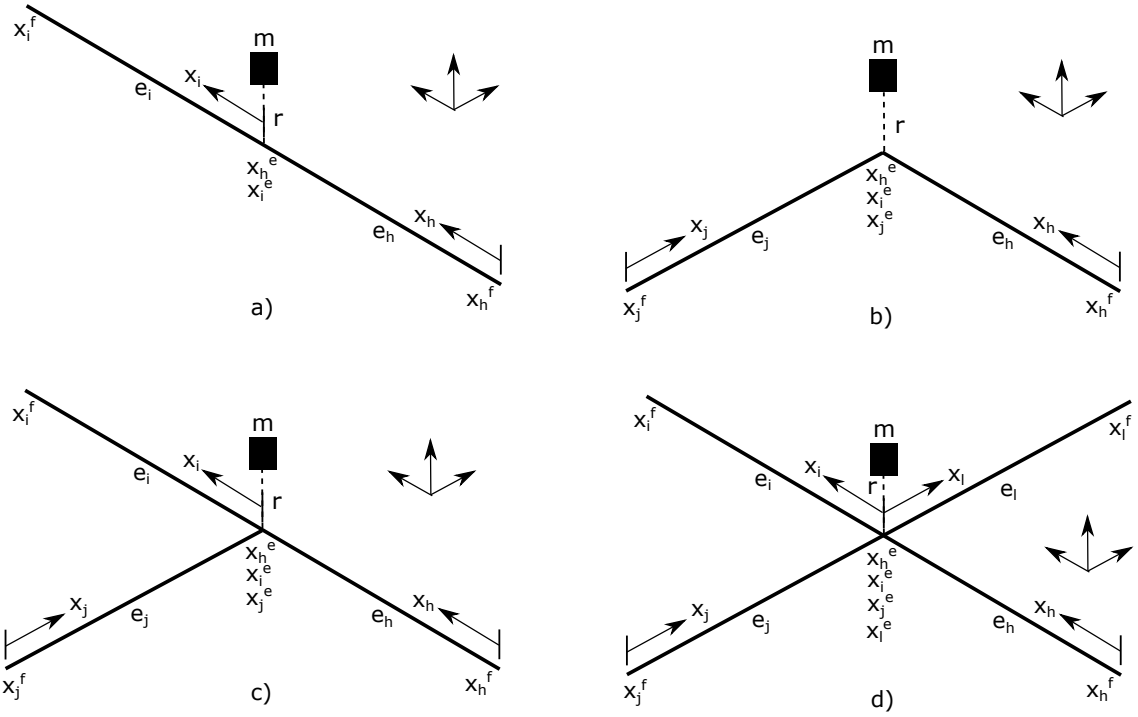

Figure 2. Different possibilities for defining initial conditions at coupling endpoints: (**a**) two aligned beams, (**b**) two perpendicular beams, (**c**) three beams, (**d**) four beams.

3.3. Modes and Fundamental Frequencies Computation

Coefficient vectors $\mathbf{c}_i$ of each beam segment $e_i \in \{e_1, e_2, ..., e_n\}$ depend on the boundary conditions of the complete structure. In detail, the set of all boundary conditions, as described in the previous section, can be rewritten as a set of coupled linear equations of the form

$$F(\omega) \begin{bmatrix} \mathbf{c}_1 \\ \mathbf{c}_2 \\ \vdots \\ \mathbf{c}_n \end{bmatrix} = \mathbf{0} \tag{19}$$

where $F(\omega)$ is a $4n \times 4n$ matrix that depends on ω. For this, it is required to substitute variables $\beta_1, \beta_2, ..., \beta_n$ in the boundary conditions by their equivalent expressions on ω, accordingly with (6), i.e.,

$$\beta_i = \left(\frac{\rho_i A_i}{E_i I_i}\right)^{1/4} \omega^{1/2}$$

Equation (19) has always a trivial solution, in which all the coefficients are null. Nevertheless, the solutions of interest appear when the coefficients are not null. For this, matrix $F(\omega)$ must lose rank, which occurs for the fundamental frequencies ω^k. These values ω^k can be obtained numerically, by using roots-finding methods such as Newton's or bisection. Next, for each of such value ω^k, the corresponding values $\{\beta_1^k, \beta_2^k, ..., \beta_n^k\}$ can be computed as in (6). Moreover, coefficients vectors $[(\mathbf{c}_1^k)^T, (\mathbf{c}_2^k)^T, ..., (\mathbf{c}_n^k)^T]^T$ can be computed fulfilling (19).

3.4. Modes for the CNC Router Structure

Let us formulate (19) for the structure of Figure 1, assuming the beams have the same cross-section and material. First, we have to define the boundary conditions as follows.

Fixed endpoints (13) in e_1, e_2, e_3 and e_4:

$$\begin{aligned} g(\beta_1,0)\mathbf{c}_1 &= 0, \quad g_x(\beta_1,0)\mathbf{c}_1 = 0,\\ g(\beta_2,l_2)\mathbf{c}_2 &= 0, \quad g_x(\beta_2,l_2)\mathbf{c}_2 = 0,\\ g(\beta_3,0)\mathbf{c}_3 &= 0, \quad g_x(\beta_3,0)\mathbf{c}_3 = 0,\\ g(\beta_4,l_4)\mathbf{c}_4 &= 0, \quad g_x(\beta_4,l_4)\mathbf{c}_4 = 0. \end{aligned}$$

Continuity at the coupled endpoints (15):

$$\begin{aligned} g(\beta_1,l_1)\mathbf{c}_1 &= g(\beta_2,0)\mathbf{c}_2,\\ g(\beta_1,l_1)\mathbf{c}_1 &= g(\beta_5,0)\mathbf{c}_5,\\ g(\beta_3,l_3)\mathbf{c}_3 &= g(\beta_4,0)\mathbf{c}_4,\\ g(\beta_3,l_3)\mathbf{c}_3 &= g(\beta_6,l_6)\mathbf{c}_6,\\ g(\beta_5,l_5)\mathbf{c}_5 &= g(\beta_6,0)\mathbf{c}_6. \end{aligned}$$

Slope continuity at the coupled endpoints between aligned beams (16):

$$\begin{aligned} g_x(\beta_1,l_1)\mathbf{c}_1 &= g_x(\beta_2,0)\mathbf{c}_2,\\ g_x(\beta_3,l_3)\mathbf{c}_3 &= g_x(\beta_4,0)\mathbf{c}_4,\\ g_x(\beta_5,l_5)\mathbf{c}_5 &= g_x(\beta_6,0)\mathbf{c}_6. \end{aligned}$$

The balance of vertical forces at coupled endpoints (17) leads to:

$$\begin{aligned} g_{xxx}(\beta_1,l_1)\mathbf{c}_1 - g_{xxx}(\beta_2,0)\mathbf{c}_2 - g_{xxx}(\beta_5,0)\mathbf{c}_5 &= -M_1\beta^4 g(\beta_1,l_1)\mathbf{c}_1,\\ g_{xxx}(\beta_3,l_3)\mathbf{c}_3 - g_{xxx}(\beta_4,0)\mathbf{c}_4 + g_{xxx}(\beta_6,l_6)\mathbf{c}_6 &= -M_2\beta^4 g(\beta_3,l_3)\mathbf{c}_3,\\ g_{xxx}(\beta_5,l_5)\mathbf{c}_5 - g_{xxx}(\beta_6,0)\mathbf{c}_6 &= -M_3\beta^4 g(\beta_5,l_5)\mathbf{c}_5, \end{aligned} \tag{20}$$

where $M_1 = m1/(\rho A)$, $M_2 = m2/(\rho A)$ and $M_3 = m3/(\rho A)$.

The balance of moments at coupled endpoints (18) leads to:

$$\begin{aligned} g_{xx}(\beta_1,l_1)\mathbf{c}_1 - g_{xx}(\beta_2,0)\mathbf{c}_2 - K^{56}(g_x(\beta_1,l_1)\mathbf{c}_1 - g_x(\beta_3,l_3)\mathbf{c}_3)&\\ = -M_1 r_1^2\beta^4 g_x(\beta_1,l_1)\mathbf{c}_1,&\\ -g_{xx}(\beta_5,0)\mathbf{c}_5 - K^{12}(g_x(\beta_5,0)\mathbf{c}_5) = -M_1 r_1^2\beta^4 g_x(\beta_5,0)\mathbf{c}_5,&\\ g_{xx}(\beta_3,l_3)\mathbf{c}_3 - g_{xx}(\beta_4,0)\mathbf{c}_4 - K^{56}(g_x(\beta_3,l_3)\mathbf{c}_3 - g_x(\beta_1,l_1)\mathbf{c}_1)&\\ = -M_2 r_2^2\beta^4 g_x(\beta_3,l_3)\mathbf{c}_3,&\\ g_{xx}(\beta_6,l_6)\mathbf{c}_6 - K^{34}(g_x(\beta_6,l_6)\mathbf{c}_6) = -M_2 r_2^2\beta^4 g_x(\beta_6,l_6)\mathbf{c}_6,&\\ g_{xx}(\beta_5,l_5)\mathbf{c}_5 - g_{xx}(\beta_6,0)\mathbf{c}_6 = -M_3 r_3^2\beta^4 g_x(\beta_5,l_5)\mathbf{c}_5,& \end{aligned} \tag{21}$$

where

$$K^{12} = \frac{GI}{EIl_1} + \frac{GI}{EIl_2},\ K^{34} = \frac{GI}{EIl_3} + \frac{GI}{EIl_4} \text{ and } K^{56} = \frac{GI}{EI(l_5+l_6)}$$

Now, if displacements are restricted to the vertical direction, additional conditions on the slopes at the coupling endpoints must hold:

$$\begin{aligned} g_x(\beta_1,l_1)\mathbf{c}_1 &= 0,\\ g_x(\beta_5,0)\mathbf{c}_5 &= 0,\\ g_x(\beta_3,l_3)\mathbf{c}_3 &= 0,\\ g_x(\beta_6,l_6)\mathbf{c}_6 &= 0. \end{aligned}$$

This will lead to a simplification of (21), since certain mass rotational inertia terms and the spring-effect terms will become null, resulting in

$$\begin{aligned}
&g_{xx}(\beta_1, l_1)\mathbf{c}_1 - g_{xx}(\beta_2, 0)\mathbf{c}_2 = 0,\\
&g_{xx}(\beta_5, 0)\mathbf{c}_5 = 0,\\
&g_{xx}(\beta_3, l_3)\mathbf{c}_3 - g_{xx}(\beta_4, 0)\mathbf{c}_4 = 0,\\
&g_{xx}(\beta_6, l_6)\mathbf{c}_6 = 0,\\
&g_{xx}(\beta_5, l_5)\mathbf{c}_5 - g_{xx}(\beta_6, 0)\mathbf{c}_6 = -M_3 r_3^2 \beta^4 g_x(\beta_5, l_5)\mathbf{c}_5.
\end{aligned}$$

The first four conditions of this set are redundant with the previous ones.

Then, the boundary conditions restricted to vertical displacements lead to the algebraic system:

$$F(\omega) = \begin{bmatrix}
g(0) & 0 & 0 & 0 & 0 & 0\\
g_x(0) & 0 & 0 & 0 & 0 & 0\\
0 & g(l_2) & 0 & 0 & 0 & 0\\
0 & g_x(l_2) & 0 & 0 & 0 & 0\\
0 & 0 & g(0) & 0 & 0 & 0\\
0 & 0 & g_x(0) & 0 & 0 & 0\\
0 & 0 & 0 & g(l_4) & 0 & 0\\
0 & 0 & 0 & g_x(l_4) & 0 & 0\\
g(l_1) & -g(0) & 0 & 0 & 0 & 0\\
g_x(l_1) & 0 & 0 & 0 & -g(0) & 0\\
0 & 0 & g(l_3) & -g(0) & 0 & 0\\
0 & 0 & g_x(l_3) & 0 & 0 & -g(l_6)\\
0 & 0 & 0 & 0 & g(l_5) & -g(0)\\
g_x(l_1) & -g_x(0) & 0 & 0 & 0 & 0\\
0 & 0 & g_x(l_3) & -g_x(0) & 0 & 0\\
0 & 0 & 0 & 0 & g_x(l_5) & -g_x(0)\\
g_{xxx}(l_1) + M_1\beta_1^4 g(l_1) & -g_{xxx}(0) & 0 & 0 & -g_{xxx}(0) & 0\\
0 & 0 & g_{xxx}(l_3) + M_2\beta_2^4 g(l_3) & -g_{xxx}(0) & 0 & g_{xxx}(l_6)\\
0 & 0 & 0 & 0 & g_{xxx}(l_5) + M_3\beta_5^4 g(l_5) & -g_{xxx}(0)\\
g_x(l_1) & 0 & 0 & 0 & 0 & 0\\
0 & 0 & 0 & 0 & g_x(0) & 0\\
0 & 0 & g_x(l_3) & 0 & 0 & 0\\
0 & 0 & 0 & 0 & 0 & g_x(l_6)\\
0 & 0 & 0 & 0 & g_{xx}(l_5) + M_3 r_3^2 \beta_5^4 g_x(l_5) & -g_{xx}(0)
\end{bmatrix}$$

$$F(\omega)\begin{bmatrix} \mathbf{c}_1\\ \mathbf{c}_2\\ \mathbf{c}_3\\ \mathbf{c}_4\\ \mathbf{c}_5\\ \mathbf{c}_6 \end{bmatrix} = \mathbf{0} \tag{22}$$

where the dependence of the functions g and theirs derivatives on ω has been omitted due to space limitations.

3.5. Modal Amplitudes in Space State

Once the modal shapes are computed, the next step is to obtain a representation of the dynamics of the modal amplitudes $T^k(t)$, for each ω^k, as function of applied loads.

Let us consider the displacement model for the i-th beam element, with an uniform damping γ and load $f(i, x_i, t)$, where $f(i, x_i, t)$ denotes the force applied on element e_i at coordinate $x_i \in [0, l_i]$ at time t:

$$E_i I_i \frac{\partial^4 w_i(x_i, t)}{\partial x_i^4} + \gamma \rho_i A_i \frac{\partial w_i(x_i, t)}{\partial t} + \rho_i A_i \frac{\partial^2 w_i(x, t)}{\partial t^2} = f(i, x_i, t) \tag{23}$$

Considering (4) and (10), it is obtained:

$$\sum_{k=1}^{\infty} W_i^k(x)\left[E_i I_i (\beta_i^k)^4\, T^k(t) + \gamma \rho_i A_i \frac{dT^k(t)}{dt} + \rho_i A_i \frac{d^2 T^k(t)}{dt^2}\right] = f(i, x_i, t)$$

Notice that modal amplitudes $T^k(t)$ do not have subindex, since each k-th modal amplitude is shared for all the beam elements.

Multiplying the previous equation by the j-th mode $W_i^j(x)$ and considering the orthogonality property $W_i^k(x_i)W_i^j(x_i) = 0$ if $k \neq j$, the following is obtained:

$$W_i^j(x_i)^2\left[E_iI_i(\beta_i^j)^4\,T^j(t)+\gamma\rho_iA_i\frac{dT^j(t)}{dt}+\rho_iA_i\frac{d^2T^j(t)}{dt^2}\right]=W_i^j(x)f(i,x_i,t)$$

The previous expression is valid for any beam element $e_i \in \{e_1, e_2, ..., e_n\}$ at any local coordinate x_i. Now, integrating over all the spatial domain (i.e., over $x_i \in [0, l_i]$ for each e_i), it is obtained:

$$\sum_{i=1}^{n}\int_0^{l_i} W_i^j(x)^2dx\left[E_iI_i(\beta_i^j)^4\,T^j(t)+\gamma\rho_iA_i\frac{dT^j(t)}{dt}+\rho_iA_i\frac{d^2T^j(t)}{dt^2}\right]$$
$$=\sum_{i=1}^{n}\int_0^{l_i} W_i^j(x)f(i,x_i,t)dx$$

Finally, using (6) and rearranging the terms, the following is obtained:

$$(\omega^j)^2\,T^j(t)+\gamma\frac{dT^j(t)}{dt}+\frac{d^2T^j(t)}{dt^2}=\frac{\sum_{i=1}^{n}\int_0^{l_i} W_i^j(x)f(i,x_i,t)dx}{\sum_{i=1}^{n}\rho_iA_i\int_0^{l_i} W_i^j(x_i)^2dx} \tag{24}$$

Equation (24) is a second-order ordinary differential equation that describes the dynamics of the j-th modal amplitude. The right-hand side is a function of time, which can be determined for different load patterns. For instance, consider that three loads are applied simultaneously, denoted as $f(i,x_i,t)=f_1(i,x_i,t)+f_2(i,x_i,t)+f_3(i,x_i,t)$, a punctual load applied on the beam element e_l, at the position $x_l = x_a$ (i.e., $f_1(i,x_i,t)=\delta_l(i)\delta(x_a)f_1(t)$, where $\delta_l(i)=1$ if $i=l$, otherwise $\delta_l(i)=0$), an uniform load with time-varying magnitude on the beam e_r (i.e., $f_2(i,x_i,t)=\delta_r(i)f_2(t)$), and an uniform constant load applied on all the beams, such as gravity (i.e., $f_3(i,x_i,t)=-gA_i\rho_i$). Then

$$\sum_{i=1}^{n}\int_0^{l_i} W_i^j(x)f_1(i,x_i,t)dx=\sum_{i=1}^{n}\int_0^{l_i} W_i^j(x_i)\delta_l(i)\delta(x_a)f_1(t)dx=W_l^j(x_a)f_1(t)$$
$$\sum_{i=1}^{n}\int_0^{l_i} W_i^j(x)f_2(i,x_i,t)dx=\sum_{i=1}^{n}\int_0^{l_i} W_i^j(x_i)\delta_r(i)f_2(t)dx=f_2(t)\int_0^{l_m} W_r^j(x_m)dx$$
$$\sum_{i=1}^{n}\int_0^{l_i} W_i^j(x)f_3(i,x_i,t)dx=\sum_{i=1}^{n}\int_0^{l_i} W_i^j(x_i)(-gA_i\rho_i)dx=-g\sum_{i=1}^{n}A_i\rho_i\int_0^{l_i} W_i^j(x_i)dx$$

Denoting, $\forall j \in \mathbb{N}$,

$$b_i^j=\int_0^{l_i} W_i^j(x_i)dx,\quad B^j=\sum_{i=1}^{n}\rho_iA_i\int_0^{l_i} W_i^j(x_i)dx,$$
$$S^j=\sum_{i=1}^{n}\rho_iA_i\int_0^{l_i} W_i^j(x_i)^2dx,\quad \eta^j=\frac{\gamma}{2\omega^j},\quad V^j(t)=\frac{dT^j(t)}{dt},$$

the expression (24) can be written as

$$\frac{dV^j(t)}{dt}=-(\omega^j)^2T^j(t)-2\eta^j\omega^jV^j(t)+\frac{W_l^j(x_a)}{S^j}f_1(t)+\frac{b_r^j}{S^j}f_2(t)-g\frac{B^j}{S^j} \tag{25}$$

The previous expression describes the dynamics of the j-th modal amplitude and its time derivative, i.e., $T^j(t)$ and $V^j(t)$.

In this way, the space state model of the first m modal amplitudes is

$$\frac{d\mathbb{T}(t)}{dt} = \begin{bmatrix} 0 & 1 & 0 & 0 & ... & 0 & 0 \\ -(\omega^1)^2 & -2\eta^1\omega^1 & 0 & 0 & ... & 0 & 0 \\ 0 & 0 & 0 & 1 & ... & 0 & 0 \\ 0 & 0 & -(\omega^2)^2 & -2\eta^2\omega^2 & ... & 0 & 0 \\ \vdots & \vdots & \vdots & \vdots & & \vdots & \vdots \\ 0 & 0 & 0 & 0 & ... & 0 & 1 \\ 0 & 0 & 0 & 0 & ... & -(\omega^m)^2 & -2\eta^m\omega^m \end{bmatrix} \mathbb{T}(t) + \begin{bmatrix} 0 & 0 & 0 \\ \frac{W_l^1(x_a)}{S^j} & \frac{b_r^1}{S^j} & \frac{B^1}{S^j} \\ 0 & 0 & 0 \\ \frac{W_l^2(x_a)}{S^j} & \frac{b_r^2}{S^j} & \frac{B^2}{S^j} \\ \vdots & & \\ 0 & 0 & 0 \\ \frac{W_l^m(x_a)}{S^j} & \frac{b_r^m}{S^j} & \frac{B^3}{S^j} \end{bmatrix} \mathbf{f}(t) \tag{26}$$

where the state is given by

$$\mathbb{T}(t) = \begin{bmatrix} T^1(t) & V^1(t) & T^2(t) & V^2(t) & ... & T^m(t) & V^m(t) \end{bmatrix}^T \tag{27}$$

and the input vector is given by

$$\mathbf{f}(t) = \begin{bmatrix} f_1(t) & f_2(t) & -g \end{bmatrix}^T \tag{28}$$

Finally, based on (10), the displacement at x_y on a beam element e_j can be approximated by considering the first m modal components as

$$w(x_y, t) \simeq \begin{bmatrix} g(\beta_j^1, x_y)\mathbf{c}_j^1 & 0 & g(\beta_j^2, x_y)\mathbf{c}_j^2 & 0 & ... & g(\beta_j^m, x_y)\mathbf{c}_j^m & 0 \end{bmatrix} \mathbb{T}(t) \tag{29}$$

The previous equation can be replicated as many times as it is required to calculate displacements at different locations.

Let us remark that there are no restrictions on the type of loads that can be applied (constant, periodic, punctual, distributed, etc.) Moreover, the simulation of the system (26)–(29) requires low computational efforts compared with numerical methods such as finite differences or *FEM*.

4. Results

In this section, numerical experiments are performed with the proposed vertical vibration model for two purposes: to validate the model, and to provide an illustrative example of the possible applications of the model. For this, a structure as shown in Figure 1 is considered.

4.1. Model Validation through Simulation

In order to validate the proposed model, fundamental frequencies and modes are computed with both our method and FEM. The goal of this comparison is to investigate the conditions under which the proposed model is valid. The choice for FEM as the ground-truth data source is due to the acceptance of the method for vibration analysis [30,31,34–36].

The analyzed structure is shown in Figure 1. The total lengths of the segments are 1 m, i.e.,

$$l_1 + l_2 = 1 \text{ m}$$
$$l_3 + l_4 = 1 \text{ m}$$

$$l_5 + l_6 = 1 \text{ m}$$

Moreover, we have the conditions $l_1 = l_3$ and $l_2 = l_4$. The cross-section of all beams is square and equal, denoting their side dimension as a, in m. Moreover, equal masses are attached to the endpoints of l_1, l_3, and l_5, as shown in Figure 1, denoting their value as m, in kg. Free endpoints are fixed, and displacements are restricted to the vertical direction.

In order to compute the fundamental frequencies ω^k, the bisection method was used to find the values ω^k at which the matrix $F(\omega^k)$, given by (22), is singular, as explained in the previous section.

For the analysis with FEM, the well-known software Ansys was used. In detail, "structural steel" was selected as the material, with a density of ρ = 7850 kg/m^3 and elastic coefficient E = 200 GPa. The torsional elastic coefficient is G = 85 N/m^2. Small high-density rigid bodies were attached (having a volume of 20 mm^3) to the endpoints of l_1, l_3, and l_5, to simulate the attached masses. Moreover, frictional supports were added to the beams lateral faces to restrict displacements to the vertical direction, as shown in Figure 3. For meshing, fine mesh with an element size of 5 mm was used, using the element "SOLID187". Smaller elements were attempted, obtaining similar results. The "Modal" analysis was performed with the "Mechanical APDL", using "Block Lanczos" as the extraction method.

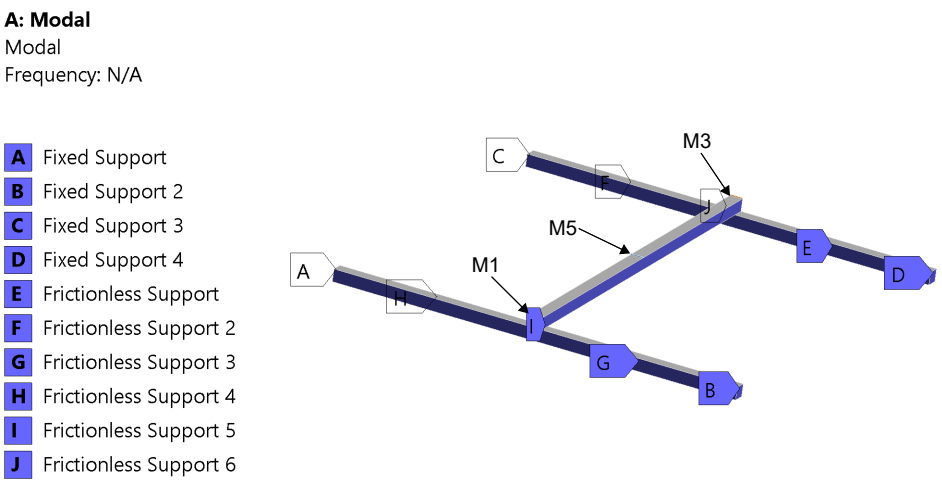

Figure 3. Structure with restrictions and attached masses for *FEM*. M1, M5 and M3 correspond to the position of mass 1, 5, and 3.

Different simulations were performed for different values of l_1, l_5, a, and m, in order to investigate the influence of each of these parameters on the solution accuracy. The following metric was used to measure the errors for the computation of the fundamental frequencies:

$$e^k(a,m) = \frac{1}{|L_1| \cdot |L_5|} \sum_{l_1 \in L_1} \sum_{l_5 \in L_5} abs\left(\frac{f^k_{Model}(l_1, l_5, a, m) - f^k_{FEM}(l_1, l_5)}{f^k_{FEM}(l_1, l_5, a, m)} \right) \tag{30}$$

where L_1 and L_5 are the set of values for l_1 and l_5, respectively, that were simulated, $f^k_{Model}(l_1, l_5, a, m)$ and $f^k_{FEM}(l_1, l_5, a, m)$ denote the k-th fundamental frequency estimated by our model and the FEM in Hertz, respectively, considering the specified values for l_1,l_5, a and m. Then, $e^k(a,m)$ represents the mean absolute proportional error of the k-th fundamental frequency.

Several simulations were performed, covering all the combinations of values $l_1 \in \{0.2, 0.3, 0.4, 0.5\}$, $l_5 \in \{0.2, 0.3, 0.4, 0.5\}$, $a \in \{0.01, 0.03, 0.1\}$ and $m \in \{0, 0.2, 1\}$. However, for the case in which $m = 0$, the value of l_5 is irrelevant. For instance, Table 1 shows the first four fundamental frequencies obtained for a = 0.01 m, m = 0.2 kg, and different values for l_1 and l_5, by using our model and FEM.

Table 1. Fundamental frequencies in Hertz obtained with our model and FEM, m = 0.2 kg, a = 0.01 m.

	l_1 = 0.2 m		l_1 = 0.3 m		l_1 = 0.4 m		l_1 = 0.5 m	
	Model	**FEM**	**Model**	**FEM**	**Model**	**FEM**	**Model**	**FEM**
l_5 = 0.2 m	45.5	48.6	36.9	39.0	29.2	30.9	26.5	28.2
	72.3	73.0	51.8	53.4	38.7	40.7	35.0	36.9
	75.7	77.2	71.4	74.9	66.7	71.2	65.6	70.3
	124.1	103.5	109.9	115.3	131.5	140.1	136.1	146.9
l_5 = 0.3 m	42.0	44.9	35.3	37.4	28.6	30.3	26.1	27.7
	72.8	73.5	52.7	54.3	39.4	41.3	35.5	37.5
	75.5	76.9	69.6	72.7	63.6	67.7	62.2	66.6
	99.3	105.6	110.2	115.7	127.4	135.8	130.0	139.5
l_5 = 0.4 m	39.3	42.0	34.0	36.1	28.1	29.8	25.8	27.4
	73.2	73.8	53.5	55.1	39.9	41.9	36.0	38.1
	75.2	76.4	66.8	69.6	59.6	63.4	58.0	61.9
	104.3	110.4	112.7	118.2	137.0	145.3	141.7	152.0
l_5 = 0.5 m	38.4	41.0	33.5	35.6	27.9	29.6	25.7	27.3
	73.3	74.0	53.8	55.4	40.2	42.1	36.3	38.3
	75.1	76.2	65.7	68.3	58.0	61.6	56.3	60.1
	106.9	113.0	113.8	119.3	143.6	151.0	153.0	164.3

Table 1 shows a good approximation of the values obtained with our model, for the case m = 0.2 kg, a = 0.01 m. Computing the mean absolute proportional error of the four fundamental frequencies, we obtain $e^1(0.01, 0.2) = 0.058$, $e^2(0.01, 0.2) = 0.035$, $e^3(0.01, 0.2) = 0.046$ and $e^4(0.01, 0.2) = 0.058$, meaning 5.8% of error for the first frequency, 3.5% of error for the second frequency, 4.6% of error for the third frequency and 5.8% for the fourth frequency.

After simulating for all the combinations of the considered parameters, the results shown in Table 2 were obtained.

Table 2. Errors obtained for the first four fundamental frequencies for all the parameters combinations.

		m = 0 kg	m = 0.2 kg	m = 1 kg
a = 0.01 m	e^1	0.064	0.058	0.059
	e^2	0.043	0.035	0.038
	e^3	0.052	0.046	0.054
	e^4	0.063	0.058	0.058
a = 0.03 m	e^1	0.082	0.073	0.073
	e^2	0.032	0.035	0.035
	e^3	0.053	0.050	0.053
	e^4	0.071	0.062	0.063
a = 0.1 m	e^1	0.084	0.099	0.198
	e^2	0.074	0.075	0.236
	e^3	0.085	0.093	0.078
	e^4	0.031	0.170	0.164

Finally, Table 3 shows the average errors for each combination of a and m, considering the first four fundamental frequencies.

Table 3. Average errors considering the first four fundamental frequencies.

	m = 0 kg	m = 0.2 kg	m = 1 kg
a = 0.01 m	0.056	0.049	0.052
a = 0.03 m	0.060	0.055	0.056
a = 0.1 m	0.069	0.109	0.169

From Table 3, it can be seen that the errors were around 5.5% for all the cases in which $a = 0.01$ m and $a = 0.03$ m, independently of the values for l_1, l_3 and m. The largest errors were obtained for $a = 0.1$ m with attached masses, i.e., with $m = 0.2$ kg and $m = 1$ kg. These results are coherent with the theory, since the Bernoulli–Euler formulation is valid for thin beams, i.e., when a is small.

Moreover, in the case of $a = 0.01$ m and $a = 0.03$ m, the mode shapes are also well approximated. For instance, Figures 4–7 show the modes associated with the first four fundamental frequencies for the case $a = 0.01$ m, $m = 1$ kg, $l_1 = 0.5$ m and $l_5 = 0.5$ m, computed with the proposed methodology and Ansys (computed modes with our model were scaled to make the highest displacements to coincide with those of FEM, note that other displacements also coincide).

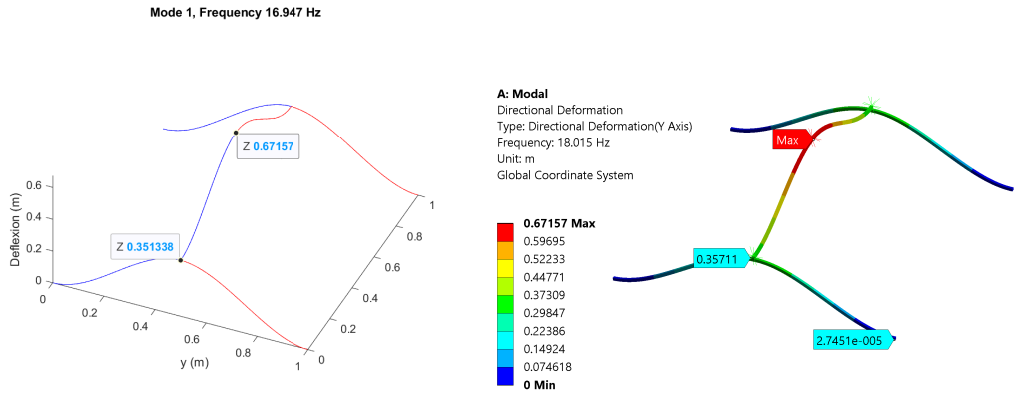

Figure 4. First mode for $a = 0.01$ m, $M = 1$ kg, $l_1 = 0.5$ m and $l_5 = 0.5$ m, computed with proposed Model (**left**) and with FEM (**right**).

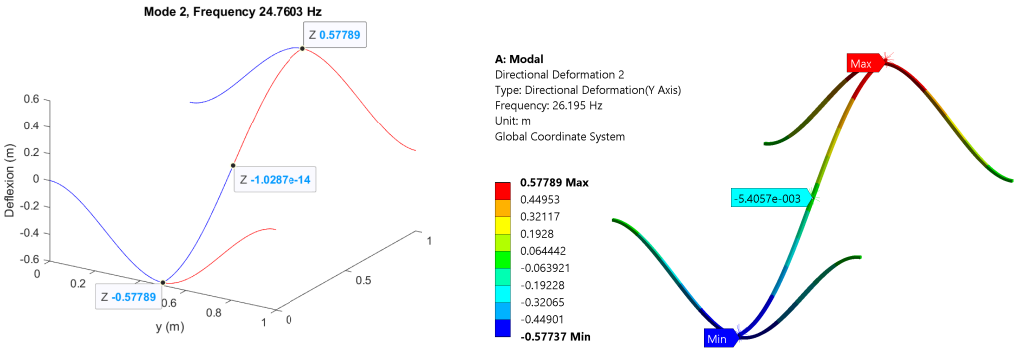

Figure 5. Second mode for $a = 0.01$ m, $M = 1$ kg, $l_1 = 0.5$ m and $l_5 = 0.5$ m, computed with proposed Model (**left**) and with FEM (**right**).

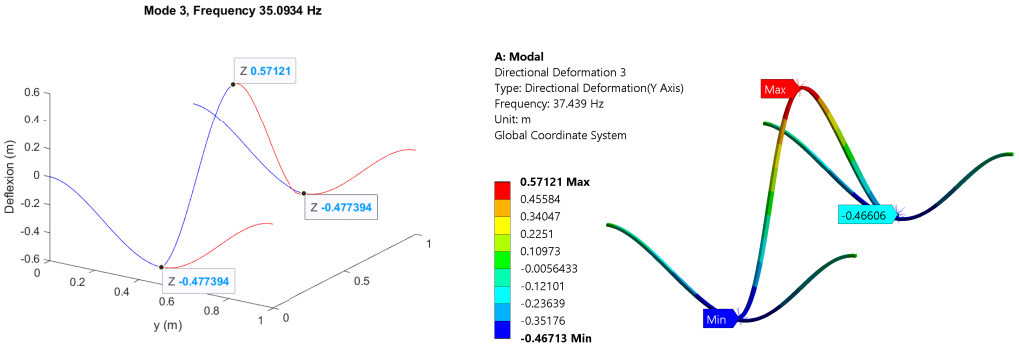

Figure 6. Third mode for $a = 0.01$ m, $M = 1$ kg, $l_1 = 0.5$ m and $l_5 = 0.5$ m, computed with proposed Model (**left**) and with FEM (**right**).

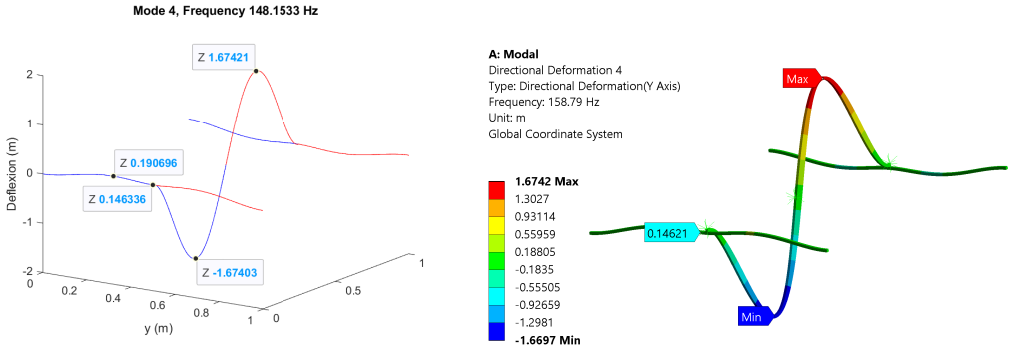

Figure 7. Fourth mode for $a = 0.01$ m, $M = 1$ kg, $l_1 = 0.5$ m and $l_5 = 0.5$ m, computed with proposed Model (**left**) and with FEM (**right**).

4.2. Model Validation through Experiments

Experimental validation was performed using the experimental setting shown in Figure 8. Considering a segmentation as in Figure 1, the total lengths of segments are such that $l_1 + l_2 = 1$ m, $l_3 + l_4 = 1$ m and $l_5 + l_6 = 0.8$ m. The structure is built with standard 20 mm $\times$ 20 mm aluminum profile with the following properties: $A = 1.6 \times 10^{-4}$ m^2, $I = 0.7 \times 10^{-8}$ m^4, $\rho = 2700$ kg/m^3, and $E = 70$ GPa. A 30 W vibration BLDC motor with a speed controller was used to induce vibrations. The minimum speed of the controller is 450 RPM. An accelerometer MPU9250 was used as a sensor device, having a bandwidth of 200 Hz. Thus, the experimental setting is able to produce and detect damped resonant frequencies in the range of 7.5 Hz–40 Hz. Consequently, only the first damped resonant frequency was investigated. Second, third, and larger resonance frequencies are not analyzed in this experiment due to practical phenomena. First, the second and larger fundamental frequencies correspond to actuator speeds larger than 4000 RPM, which are not excited in practical CNC router machines. Moreover, magnitudes associated with the second and larger fundamental frequencies are several times smaller than that of the first fundamental frequency. Furthermore, when damping exists (i.e., when considering real structures), second and larger resonance frequencies tend to vanish, thus making it impractical to detect those frequencies in experimental settings. Different simulations were performed, characterized by the combinations of values $l_1 \in \{0.2, 0.3, 0.4, 0.5\}$ and $l_5 \in \{0.2, 0.4\}$. For instance, Figure 9 shows the vertical accelerations obtained (in g units) for different load frequencies (motor speed). The first damped resonant frequencies are shown in Table 4 (indicated as exp.)

Simulations based on the proposed model were performed for the same combinations, applying harmonic loads with a frequency in the interval 0 Hz–50 Hz to estimate the first damped resonant frequency. For this, a damping coefficient of $\gamma = 0.3$ was considered. Masses were considered as $m_1 = m_2 = 0.45$ kg and $m_3 = 2.9$ kg, with $r_1 = r_2 = 0$ and $r_3 = 0.035$ m, associated to the motor and other accessories. The obtained first damped resonant frequencies are shown in Table 4, together with the resulting absolute percentage errors. The error of the first frequency is below 0.05 for the cases with $l_1 = 0.4$ m and $l_1 = 0.5$ m. Similarly, the error is below 0.15 in all the cases in which $l_5 = 0.4$ m. The largest error (0.375) was obtained with the configuration ($l_1 = 0.2$ m, $l_5 = 0.2$ m). Notice that the error becomes larger when the structure reaches a position with larger rigidity (where the motor is closer to a corner), in which vibration amplitudes are expected to be smaller. The average error is 0.108. In this way, we consider that the experiments validate that the proposed model provides a fair approximation of the first resonance frequency, specially at the less rigid positions in which vibration amplitudes are expected to be more relevant.

Figure 8. Structure for experimental validation (**left**) and detail of the aluminum profile (**right**).

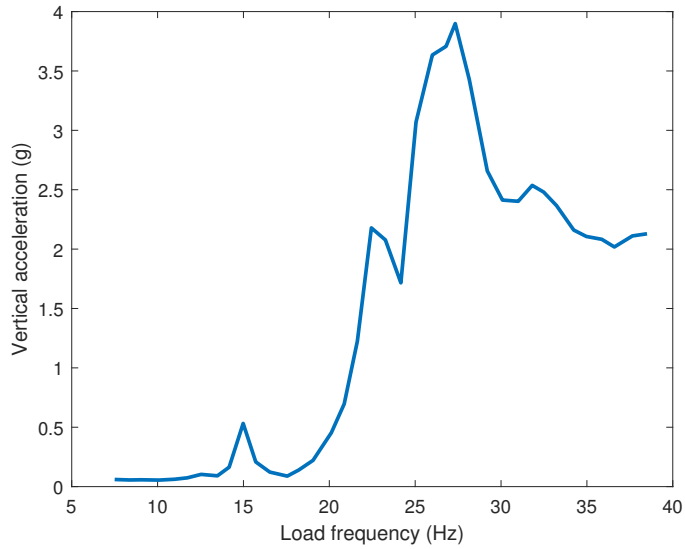

Figure 9. Experimental results for the case $l_1 = 0.4$ m, $l_5 = 0.2$ m. The peak acceleration occurs at 27.33 Hz.

Table 4. First damped resonant frequency in Hertz obtained with the experimental setting (exp.) and our model. The average error is 0.108.

		$l_1 = 0.2$ m	$l_1 = 0.3$ m	$l_1 = 0.4$ m	$l_1 = 0.5$ m
$l_5 = 0.2$ m	exp.	32.58	28.30	27.33	24.96
	model	44.8	34.0	26.8	24.4
	error	0.375	0.201	0.019	0.022
$l_5 = 0.4$ m	exp.	29.08	28.46	25.80	24.83
	model	33.4	29.4	25.4	23.6
	error	0.148	0.033	0.015	0.049

5. Discussion

In order to illustrate different applications of the proposed model, we perform an analysis of a CNC structure similar as the structure shown in Figure 1. The frequencies and modes depend solely on the material and geometry parameters. These parameters are sourced from the manufacturer of the CNC *router* type being modeled. If not available, they can be easily measured. For amplitudes, damping is required. The damping can be adjusted from experimentation. We assume that the structure is built with standard 40 mm $\times$ 20 mm aluminum profiles as shown in Figure 10, having the following parameters: $A = 3.405 \times 10^{-4}$ m^2, $I = 5.4113 \times 10^{-8}$ m^4, $\rho = 2700$ kg/m^3, $E = 70$ GPa. A damping coefficient of $\gamma = 0.04$ was considered.

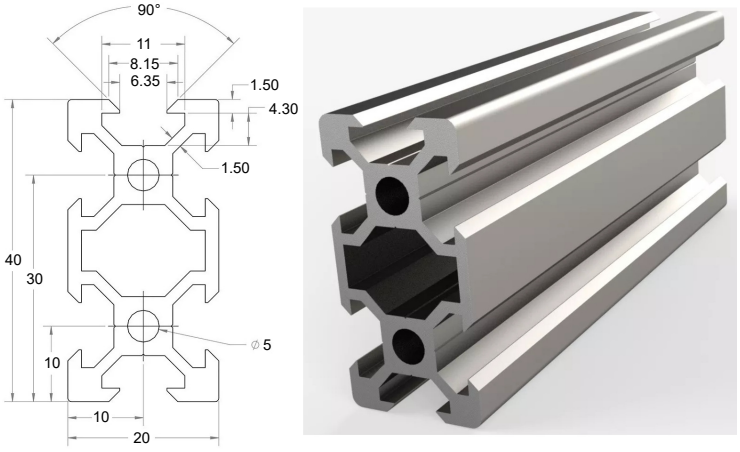

Figure 10. Standard aluminum profile, 40 mm × 20 mm.

Considering the structure decomposition as in Figure 1, attached masses are considered at the coupling endpoints of e_1 and e_3, representing motors NEMA23 with masses $m_1 = m_2 = 1.15$ kg and a vertical distance between the mass centers and the neutral axis of $r_1 = r_2 = 0.06$ m. Moreover, a third mass is attached at the end of e_5, representing the Z-axis displacement mechanism and a spindle, involving a total mass of $m_3 = 12.5$ kg with $r_3 = 0.06$ m. In this way, the masses, material, and cross-section parameters are defined.

Notice that the length of the beam elements depends on the X–Y spindle position, which changes according to the manufacturing program. The total length of the X-axis profiles is 1 m, and the total length of the Y-axis profiles is 0.8 m, i.e., $l_1 + l_2 = l_3 + l_4 = 1$ m and $l_5 + l_6 = 0.8$ m.

The first analysis approach is to compute a map of fundamental frequencies, as shown in Figure 11. These maps are computed by building the model for different values of l_1 and l_5, representing the X–Y position of the spindle, and computing the corresponding fundamental frequencies. As expected, the lower frequencies are found when the spindle is at the center of the CNC range, i.e., when m_3 is farthest from the fixed endpoints. On the other hand, the fundamental frequencies are larger when l_1 is near 0 m or 1 m, i.e., when the spindle is near the CNC supports, since the structure becomes more rigid at these configurations.

These maps could be used by open-loop control strategies to avoid excessive vibrations. For instance, the spindle speed may be shifted away from the fundamental frequencies, depending on the spindle position. Moreover, when working on a small piece, this could be placed in the region where the first frequencies are high (the higher the frequency, the lower the vibration displacement).

In a second analysis, a map of vertical displacements is performed, as shown in Figure 12 (left). This map indicates the vertical displacement of the spindle for different X–Y positions (i.e., for different values of l_1 and l_5), when a load of $f(t) = -100N$ is applied on the spindle. This map is computed by building the model for different values of l_1 and l_5, including their state space representations of the modal amplitudes for the first four fundamental frequencies, and computing the steady state of the corresponding models. The map can be used at a design stage, in order to analyze the magnitude of the vertical deflection at a constant load (for instance, the weight of the tool) and determine whether the difference between the minimum and maximum deflections is permissible. In this case, the difference was over 3 mm, which would affect the piece quality. Figure 12 (right) shows the steady-state displacements of all the structures for the case in which $l_1 = 0.1$ m, $l_5 = 0.45$ m, which was computed by using the steady-state modal amplitudes and the mode shapes.

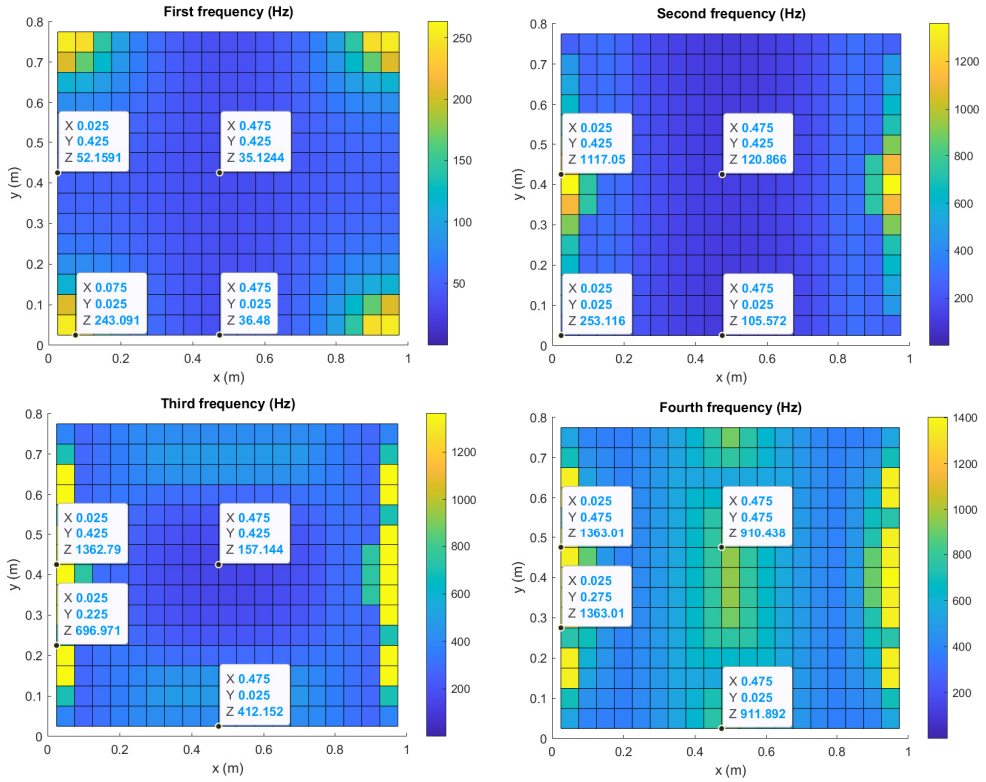

Figure 11. First four fundamental frequencies. X–Y axis represents the coordinate of the spindle.

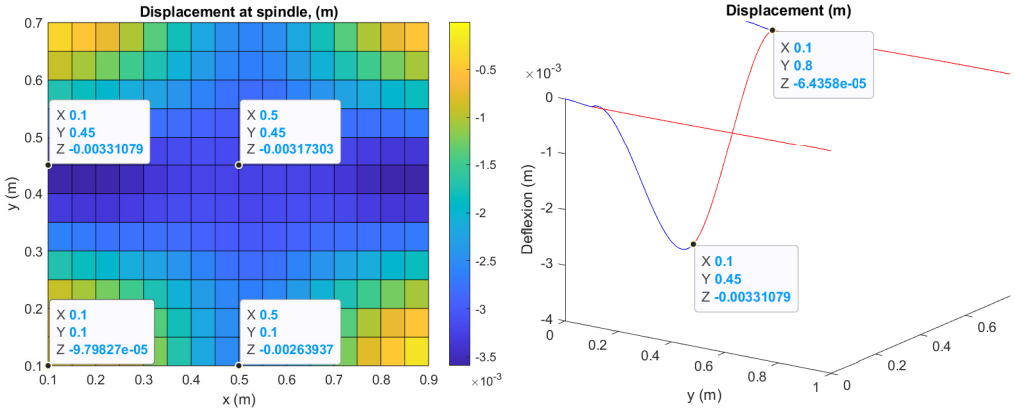

Figure 12. (**Left**) steady- state displacement at the spindle, for different positions of this. (**Right**) steady-state displacement displacements of the structure for the case l_1 = 0.1 m, l_5 = 0.45 m. In both results, a constant load of $f(t) = -100N$ was applied at the spindle position.

In a third analysis, the behavior of the structure is studied when a harmonic load of $f(t) = -100sin(2\pi f_c t)\ N$ is applied, where the load frequency is varied in the range $f_c \in [0, 300]$ Hz. Figure 13 (left) shows the amplitude of the displacement at the spindle, for the different values of f_c, for the case in which l_1 = 0.5 m and l_5 = 0.4 m. This type of analysis allows us to detect the frequencies of maximum displacements (damped resonant frequency) at particular configurations (which are expected to be near the fundamental frequencies, depending on the damping coefficient), and the displacement differences between different damped resonant frequencies. In this case, we only need to consider the first frequency (near 35 Hz), since the displacement magnitudes at the others are negligible.

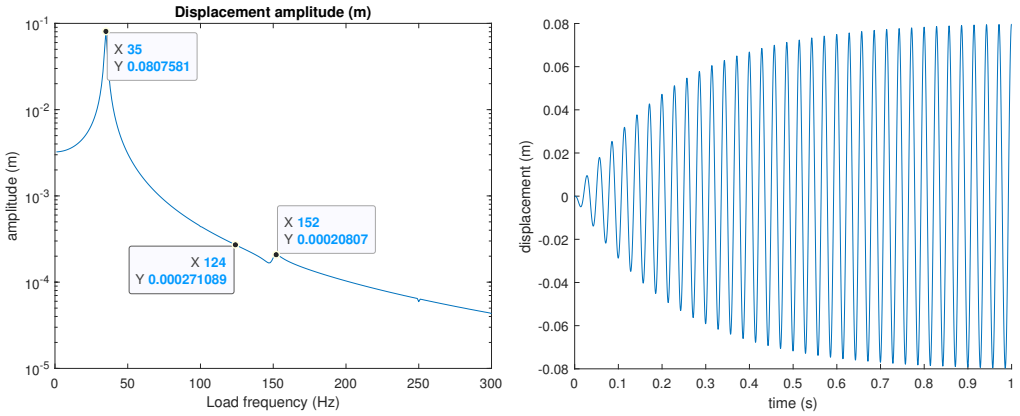

Figure 13. (**Left**) displacement amplitude at the spindle for the periodic load $f(t) = -100sin(2\pi f_c t)\ N$, for the case l_1 = 0.1 m, l_5 = 0.45 m. (**Right**) transient displacement at the spindle for the case f_c = 35 Hz.

Finally, Figure 13 (right) shows the transient behavior of the displacements at the spindle for the case $f_c = 35$ Hz, i.e., at the first damped resonant frequency. This displacement plot was obtained by a simple simulation of the modal amplitude state space. The simulation was performed in discrete time using the Euler rule with a sampling of 0.5 ms. This model would be useful for designing and implementing model-based control algorithms for reducing vibrations (e.g., using a piezoelectric actuator to slightly move the working piece to suppress the displacement).

6. Conclusions

In this study, an analytical methodology to calculate the vibration modes of coupled thin beams is presented. This methodology is applied to estimate the vertical vibrations of a CNC *router* type machine. It is of interest to obtain analytical models for the vertical vibrations of this machine type to avoid problems with the tool and the machined surface. The validation results reveal a small error for the first fundamental frequencies using the method compared with FEM simulations, whenever the cross-sectional areas of the beams are small with respect to their lengths (Bernoulli–Euler hypothesis). Furthermore, the qualitative behavior of the first four vibration modes is similar using both methods. Moreover, experimental validation was performed with a small cross-sectional area beam structure, obtaining an average error of 0.10 considering different positions, and exhibiting greater accuracy at less rigid positions where vibration amplitudes are expected to be more relevant. To illustrate the application of the method, this was applied to model vertical vibrations in a CNC *router* type geometry. As such, the first natural frequencies were computed for different positions of the tool. Moreover, displacements were computed for a constant and a dynamic load. Application of the obtained analytical model for control and predictive maintenance remains a topic for future work.

Author Contributions: Conceptualization, C.R.V.; Methodology, C.R.V.; Formal analysis, C.R.V. and A.G.-C.; Investigation, C.R.V. and A.G.-C.; Writing—original draft, C.R.V.; Writing—review & editing, A.G.-C. All authors have read and agreed to the published version of the manuscript.

Funding: This research received no external funding.

Institutional Review Board Statement: Not applicable.

Informed Consent Statement: Not applicable.

Data Availability Statement: Data is contained within the article.

Conflicts of Interest: The authors declare no conflicts of interest.

Abbreviations

The following abbreviations are used in this manuscript:

CNC	Computer Numerical Control
FEM	Finite Element Method

References

1. Minis, I.; Yanushevsky, R. A new theoretical approach for the prediction of machine tool chatter in milling. *J. Manuf. Sci. Eng.* **1993**, *115* , 1–8. [CrossRef]
2. Altintaş, Y.; Budak, E. Analytical prediction of stability lobes in milling. *CIRP Ann.* **1995**, *44*, 357–362. [CrossRef]
3. Ghoshal, B.; Bhattacharyya, B. Influence of vibration on micro-tool fabrication by electrochemical machining. *Int. J. Mach. Tools Manuf.* **2013**, *64*, 49–59. [CrossRef]
4. Quintana, G.; Ciurana, J. Chatter in machining processes: A review. *Int. J. Mach. Tools Manuf.* **2011**, *51*, 363–376. [CrossRef]
5. Jensen, S.A.; Shin, Y.C. Stability Analysis in Face Milling Operations, Part 1: Theory of Stability Lobe Prediction. *J. Manuf. Sci. Eng.* **1999**, *121*, 600–605. [CrossRef]
6. Jensen, S.A.; Shin, Y.C. Stability Analysis in Face Milling Operations, Part 2: Experimental Validation and Influencing Factors. *J. Manuf. Sci. Eng.* **1999**, *121*, 606–614. [CrossRef]
7. Budak, E.; Altintas, Y. Analytical Prediction of Chatter Stability in Milling—Part I: General Formulation. *J. Dyn. Syst. Meas. Control* **1998**, *120*, 22–30. [CrossRef]
8. Long, X.; Jiang, H.; Meng, G. Active vibration control for peripheral milling processes. *J. Mater. Process. Technol.* **2013**, *213*, 660–670. [CrossRef]
9. Aggogeri, F.; Al-Bender, F.; Brunner, B.; Elsaid, M.; Mazzola, M.; Merlo, A.; Ricciardi, D.; De La O Rodriguez, M.; Salvi, E. Design of piezo-based AVC system for machine tool applications. *Mech. Syst. Signal Process.* **2013**, *36*, 53–65. [CrossRef]
10. Ostasevicius, V.; Gaidys, R.; Rimkeviciene, J.; Dauksevicius, R. An approach based on tool mode control for surface roughness reduction in high-frequency vibration cutting. *J. Sound Vib.* **2010**, *329*, 4866–4879. [CrossRef]
11. Altintas, Y.; Khoshdarregi, M.R. Contour error control of CNC machine tools with vibration avoidance. *CIRP Ann.* **2012**, *61*, 335–338. [CrossRef]
12. Ford, D.G.; Myers, A.; Haase, F.; Lockwood, S.; Longstaff, A. Active vibration control for a CNC milling machine. *Proc. Inst. Mech. Eng. Part C J. Mech. Eng. Sci.* **2014**, *228*, 230–245. [CrossRef]
13. Lei, Y.; Li, N.; Guo, L.; Li, N.; Yan, T.; Lin, J. Machinery health prognostics: A systematic review from data acquisition to RUL prediction. *Mech. Syst. Signal Process.* **2018**, *104*, 799–834. [CrossRef]
14. Rezaeianjouybari, B.; Shang, Y. Deep learning for prognostics and health management: State of the art, challenges, and opportunities. *Measurement* **2020**, *163*, 107929. [CrossRef]
15. Ding, A.; Qin, Y.; Wang, B.; Jia, L.; Cheng, X. Lightweight Multiscale Convolutional Networks With Adaptive Pruning for Intelligent Fault Diagnosis of Train Bogie Bearings in Edge Computing Scenarios. *IEEE Trans. Instrum. Meas.* **2023**, *72*, 1–13. [CrossRef]
16. Routakit CNC. Available online: https://www.kickstarter.com/projects/lumacco/routakit (accessed on 18 April 2023).
17. PRO60120 CNC. Available online: https://www.avidcnc.com/pro60120-5-x-10-cnc-router-kit-p-374.html (accessed on 18 April 2023).
18. X-Carve CNC. Available online: https://www.inventables.com/technologies/x-carve (accessed on 18 April 2023).
19. Zenbot CNC. Available online: https://www.zenbotcnc.com/ (accessed on 18 April 2023).
20. Luo, G.; Osypiw, D.; Irle, M. Surface quality monitoring for process control by on-line vibration analysis using an adaptive spline wavelet algorithm. *J. Sound Vib.* **2003**, *263*, 85–111. [CrossRef]
21. Liu, H.; Lu, D.; Zhang, J.; Zhao, W. Receptance coupling of multi-subsystem connected via a wedge mechanism with application in the position-dependent dynamics of ballscrew drives. *J. Sound Vib.* **2016**, *376*, 166–181. [CrossRef]
22. Biantoro, A.; Maryanto, H.; Hidayanto, A.; Hamid, A. The investigation of end mill feeds on CNC router machine using vibration method. *Sinergi* **2020**, *24*, 117–124. [CrossRef]
23. Tran, V.T.; Nguyen, H.L.; Nguyen, H.H. Analysis and Experimental Design of Damper System and Cutting Parameters of CNC Router. In *Proceedings of the Applied Mechanics and Materials*; Trans Tech Publications: Stafa-Zurich, Switzerland, 2019; Volume 894, pp. 82–89.
24. Huu Loc, N.; Van Thuy, T. The Effects of Bolt Preload on Vibration Amplitude of Gantry CNC Router. *Int. J. Mech. Eng. Technol.* **2019**, *10*, 323–332.
25. Loc, N.H.; Hung, N.P. Utilizing response surface methods designs for optimization of technological parameters on the vibration amplitude of CNC router spindle. *ASEAN Eng. J.* **2021**, *11*, 34–44. [CrossRef]
26. Kukla, S.; Posiadala, B. Free Vibrations of Beams with Elastically Mounted Masses. *J. Sound Vib.* **1994**, *175*, 557–564. [CrossRef]
27. Kukla, S. Free Vibrations of Axially Loaded Beams With Concentrated Masses and Intermediate Elastic Supports. *J. Sound Vib.* **1994**, *172*, 449–458. [CrossRef]
28. Ghayesh, M.H.; Kazemirad, S.; Darabi, M.A. A general solution procedure for vibrations of systems with cubic nonlinearities and nonlinear/time-dependent internal boundary conditions. *J. Sound Vib.* **2011**, *330*, 5382–5400. [CrossRef]

29. Rezaiee-Pajand, M.; Hozhabrossadati, S.M. Free vibration analysis of a double-beam system joined by a mass-spring device. *J. Vib. Control* **2016**, *22*, 3004–3017. [CrossRef]
30. Wu, C.C. Free vibration analysis of a free-free Timoshenko beam carrying multiple concentrated elements with effect of rigid-body motions considered. *J. Sound Vib.* **2019**, *445*, 204–227. [CrossRef]
31. Liu, X.; Sun, C.; Ranjan Banerjee, J.; Dan, H.C.; Chang, L. An exact dynamic stiffness method for multibody systems consisting of beams and rigid-bodies. *Mech. Syst. Signal Process.* **2021**, *150*, 107264. [CrossRef]
32. Maiz, S.; Bambill, D.V.; Rossit, C.A.; Laura, P.A.A. Transverse vibration of Bernoulli–Euler beams carrying point masses and taking into account their rotatory inertia: Exact solution. *J. Sound Vib.* **2007**, *303*, 895–908. [CrossRef]
33. Maiz, S.; Rossit, C.A.; Bambill, D.V. Consideración De Distintas Teorías En La Vibración De Vigas Con Masas Adosadas. *Mec. Comput.* **2007**, *ZZXK*, 278–297.
34. Petyt, M. *Introduction to Finite Element Vibration Analysis*; Cambridge University Press: Cambridge, UK, 2010.
35. Rao, D.K.; Blessington, P.; Tarapada, R. Finite element modeling and analysis of functionally graded (FG) composite shell structures. *Procedia Eng.* **2012**, *38*, 3192–3199. [CrossRef]
36. Ozer, M.S.; Koruk, H.; Sanliturk, K.Y. Testing non-magnetic materials using Oberst Beam Method utilising electromagnetic excitation. *J. Sound Vib.* **2019**, *456*, 104–118. [CrossRef]